remote sensing

MDPI

Article

On-Orbit Radiometric Calibration for a Space-Borne Multi-Camera Mosaic Imaging Sensor

Yong Xie [1], Jie Han [2,*], Xingfa Gu [3] and Qiyue Liu [3]

[1] School of Geography and Remote Sensing, Nanjing University of Information Science & Technology, Nanjing 210044, China; xieyong@nuist.edu.cn
[2] School of Urban-Rural Planning and Architecture, Xuchang University, Xuchang 461000, China
[3] State Key Laboratory of Remote Sensing Science, Institute of Remote Sensing and Digital Earth, Chinese Academy of Sciences, Beijing 100101, China; guxingfa@radi.ac.cn (X.G.); liuqy@radi.ac.cn (Q.L.)
* Correspondence: hanjie@radi.ac.cn; Tel.: +86-374-2968710

Received: 3 November 2017; Accepted: 28 November 2017; Published: 1 December 2017

Abstract: As the core and foundational technology, on-orbit radiometric calibration of a space-borne sensor is of great importance for quantitative remote sensing applications. As for the space-borne multi-camera mosaic imaging sensor, however, the currently available on-orbit radiometric calibration method cannot carry out the integrated processing of on-orbit absolute radiometric calibration and relative radiometric correction simultaneously between cameras, influencing the accuracy of quantitative applications. Therefore, taking the GaoFen-1 (GF-1) wide-field-of-view (WFV) sensor as an example in this research, an innovative on-orbit radiometric calibration method is proposed to overcome this bottleneck. Firstly, according to the principle of the cross-calibration approach, we retrieve valid MODIS and GF-1 WFV image pairs over the Dunhuang radiometric calibration sites (DRCS) in China by using a set of criteria and extract the radiometric control points (RCPs) connecting in both images. Secondly, the DEM-aided block adjustment of the rational function model is applied to eliminate the geometrical misalignment of GF-1 WFV images at the same orbit. Then, the average digital numbers of spectral and spatial homogeneous surfaces are calculated and chosen as the radiometric tie points (RTPs) extracted from the overlapping region of the adjacent WFV cameras. Thirdly, the radiometric block adjustment (RBA) algorithm is introduced into on-orbit radiometric calibration of the space-borne multi-camera mosaic imaging sensor. Finally, the radiometric calibration coefficients are solved by the least square method. The validation results indicate that our proposed method can acquire high absolute radiometric calibration accuracy and achieve relative radiometric correction between cameras. Compared with the results using the cross-calibration method to calibrate each WFV camera independently, the advantages of RBA are presented. In addition, the uncertainties caused by RCPs' distribution are discussed, which is beneficial to further optimize the calibration program.

Keywords: on-orbit radiometric calibration; multi-camera mosaic imaging; radiometric block adjustment; validation and evaluation

1. Introduction

Radiometric calibration is an important process that converts the digital number (DN) of the Earth observation sensor to the at-sensor spectral radiance or the top-of-atmosphere (TOA) reflectance, which is one of the research hotspots in quantitative remote sensing. It is known that the radiometric characteristics of the sensor will change due to outgassing, the electronic system deterioration, the spectral response variation, etc. [1]. Therefore, on-orbit radiometric calibration is a crucial step for quantitative remote sensing applications, which can monitor the radiometric performance changes of the sensor and estimate the radiometric quality and stability during the operation period. It also

can ensure that the phase change information of the surface is able to be detected by the sensor rather than be covered with the radiometric degradation of the sensor. Moreover, the different radiometric observation information can be normalized into a common radiometric scale by the radiometric calibration, which can provide a better basis for the comparison of data between images taken from different acquisition dates and/or by multiple sensors [2,3].

It is difficult to obtain an image with a large swath and high spatial resolution satellite simultaneously for a single camera. An image from a single camera with high spatial resolution but narrow swath might be wide enough to be acceptable for a small application region, but not for a large application area. In order to overcome this obstacle, the multi-camera mosaic imaging technique currently is applied to integrate several high resolution cameras to achieve a large-swath image with a slight overlap between each adjacent camera pair along the scan direction. When applying images of multi-camera mosaic imaging sensor to a quantitative remote sensing application for a large region, images of adjacent cameras on the same track will be spliced to get a large-swath satellite image with high resolution, which is a major development aim of this type of sensor. Meanwhile, the number of available images is less due to the lower time resolution without satellite side-swing and the cloud coverage. If the research region is located at the overlapping area of adjacent camera, in order to increase the access efficiency, the adjacent camera images also must be spliced to get the mosaicking image of the whole region of interest.

Presently, the in situ calibration method [1,4], the cross-calibration method [3,5] and the onboard calibration method [6,7] are popular. In China, the official calibration coefficients (OCCs) of civil satellites are obtained by using the in situ calibration at the Dunhuang radiometric calibration sites (DRCS). However, obvious radiometric differences in the overlapping area of adjacent cameras are calculated with OCCs, hence severely affecting the application effect for this type of sensor imagery [8]. The radiometric normalization method is used to solve the problem [9,10]. However, those processing procedures will destroy the original radiometric information, which will reduce the credibility and accuracy of the subsequent quantitative remote sensing production. As for the on-orbit radiometric calibration of the space-borne multi-camera mosaic imaging sensor, the radiation coherence constraint between adjacent cameras must be considered to assure that the radiation differences in the overlapping area are down to the minimum.

The wide-field-of-view (WFV) sensor of the GF-1 satellite is a typical multi-camera mosaic imaging sensor and is selected as a candidate to be calibrated in our study. The radiometric block adjustment (RBA) algorithm is introduced into the on-orbit radiometric calibration of the GF-1 WFV sensor. The innovative radiometric calibration method is proposed to realize the integrated processing of on-orbit absolute radiometric calibration and relative radiometric correction between cameras, which will enlarge the application filed for this type of sensor.

The organization of this paper is as follows: GF-1 WFV, MODIS, the test sites and datasets are described in Section 2. Section 3 introduces the principle and previous research of RBA, the methods of radiometric control points' (RCPs) and radiometric tie points' (RTPs) extraction and the details of the innovative radiometric calibration method. Results of radiometric calibration and verification of the accuracy of absolute radiometric calibration and relative radiometric correction between cameras are illustrated in Section 4. Section 5 compares the results of RBA and the traditional cross-calibration and discusses the influence of the RCPs' distribution on the calibration accuracy. Section 6 is a summary and conclusion of our research.

2. Satellites, Test Sites and Datasets

2.1. Satellites

The GF-1 satellite is the first satellite in the Chinese High-resolution Earth Observation System (CHEOS), which was launched on 26 April 2013. It accommodates a panchromatic and multispectral (PMS) sensor and a WFV sensor, both of which are designed to provide optical push-broom imagery [5,8,11].

From its configuration shown in Figure 1 [12], the WFV sensor is very representative of a space-borne multi-camera mosaic imaging sensor in CHEOS because it is integrated with four cameras to achieve an 800-km splicing swath at a 16-m spatial resolution. The view angle of each camera's principal optic axis is approximately 16° apart. Each camera has four bands (450 nm–520 nm blue, 520 nm–590 nm green, 630 nm–690 nm red and 770 nm–890 nm near-infrared), and its data are quantized into 10 bit. The revisit time, determining the calibration frequency, is around four days without platform side-sway.

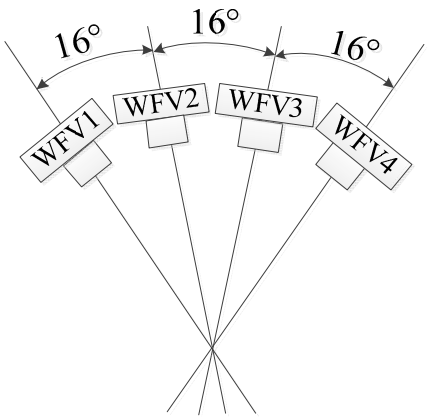

Figure 1. Wide-field-of-view (WFV) sensor configuration.

MODIS aboard the Terra satellite was launched on 18 December 1999, which freely provides near-daily global coverage data quantized into 12 bit [6]. The solar diffuser (SD) and solar diffuser stability monitor (SDSM) can ensure the uncertainty of MODIS TOA reflectance products and at-sensor spectral radiance products is around 2% and 5%, respectively [5,7]. MODIS, therefore, is acting as the radiance reference for on-orbit cross-calibration of space-borne sensors absent an on-orbit radiometric calibration facility. In our research, Band 3 (459 nm–479 nm), Band 4 (545 nm–565 nm), Band 1 (620 nm–670 nm) and Band 2 (841 nm–876 nm) of the MOD02HKM, Level-1b product with a 500-m ground sample distance are used to extract the radiance reference information.

Figure 2 illustrates the Band 1–4 relative spectral responses (RSR) of WFV and MODIS, which reveals that the RSRs of four WFV cameras are very similar to each other and different from the RSR of MODIS. Therefore, this status should be considered in the radiance information extraction.

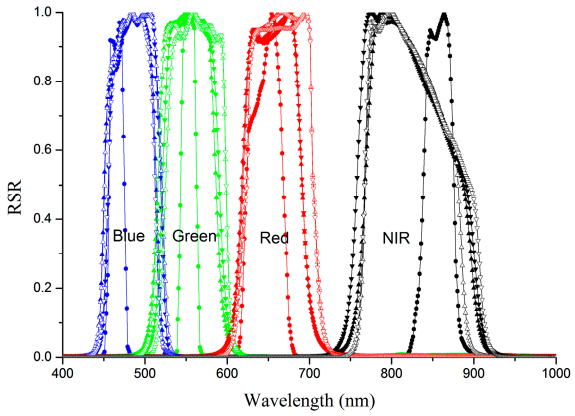

Figure 2. The Band 1–4 relative spectral responses (RSR) of WFV and the MODIS sensor. The solid upward triangle lines, the solid downward triangle lines, the hollow upward triangle lines, the hollow downward triangle lines and the solid circle lines represent the RSR of WFV1, WFV2, WFV3, WFV4 and MODIS, respectively.

2.2. Test Sites

DRCS is an important radiometric calibration site in China, which has been widely recognized internationally due to its flat terrain, homogeneous surface and good radiation direction shown in Figure 3 [13]. The coefficient of variation (CV) (the ratio of the standard deviation and mean reflectance) of reflectance over DRCS is about 5% [5]. This site is officially used to obtain on-orbit absolute radiometric calibration coefficients for the visible and near-infrared sensor of Chinese land observation satellites by using the vicarious calibration method, such as the CBERS (China and Brazil Earth Resource Satellite), HJ (HuanJing), FY (FengYun), ZY (ZiYuan), GF-1, GF-2, GF-4, TH (TianHui), etc. [14–17]. DRCS is located about 25 km west of Dunhuang City in Gansu province. The latitude and longitude range is about 40.04°N–40.28°N, 94.17°E–94.5°E, and the altitude is up to 1200 m.

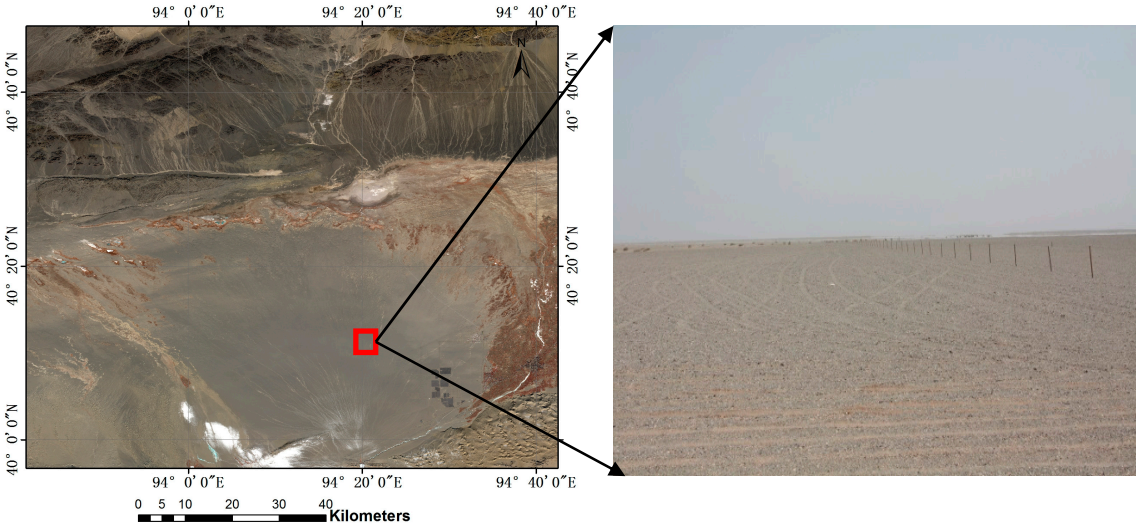

Figure 3. The Dunhuang test site.

2.3. Datasets

The effective collection of synchronous or quasi-synchronous image pairs of WFV and MODIS is crucial for radiometric control information. In our research, the track intersection prediction algorithm is introduced to obtain the WFV and MODIS images passing over the DRCS in the same day. Then, the following criteria act as the data filter and are applied to acquire the valid images. (a) The overpass time gap between MODIS and WFV is less than 1 h, for which it can be assumed that the atmospheric and surface conditions did not change significantly [1]. (b) The image is uncontaminated by cloud clusters, which will damage the spectral and spatial characteristic of the DRCS in image [18]. (c) The WFV image should cover the center region of the DRCS where there is more spectral and spatial homogeneity [13,17]. (d) The DRCS should not be located at the edge of the MODIS image, which can reduce the influence of the "bow tie" effect [19].

After being launched on 26 April 2013, the GF-1 satellite first underwent an important six-month commissioning phase period, which could improve the geometric and radiometric quality of the image to meet the demanding specification. Therefore, under these criteria, we retrieve the Terra MODIS and WFV image over the DRCS from October 2013–April 2015. Results show that after being filtered by the above criteria, the number of valid image pairs is not equal for each WFV camera: 5 for WFV1, 6 for WFV2, 6 for WFV3 and 9 for WFV4. The information of the collocated imagery is listed in Table 1. Figure 4 shows that the view angles for DRCS in the WFV and MODIS images are quite different, so that the bidirectional reflectance distribution function (BRDF) characteristic of DRCS needs to be taken into account [14,17].

Table 1. Information of valid WFV and MODIS imageries.

No.	Date Since Launched/Day	GF-1 Camera	WFV Time	MODIS Time	△t/′
1	214	WFV1	12:33	13:00	27
2	276	WFV1	12:37	12:30	7
3	312	WFV1	12:46	12:45	1
4	332	WFV1	12:36	12:25	11
5	731	WFV1	12:55	12:26	29
6	240	WFV2	12:50	12:55	5
7	244	WFV2	12:48	12:30	18
8	301	WFV2	12:50	12:25	25
9	637	WFV2	13:00	12:25	35
10	674	WFV2	13:03	12:40	23
11	715	WFV2	13:04	12:35	29
12	534	WFV3	13:08	13:00	8
13	575	WFV3	13:10	12:55	15
14	616	WFV3	13:11	12:45	26
15	657	WFV3	13:12	12:40	32
16	662	WFV3	13:10	12:15	55
17	669	WFV3	13:13	12:35	38
18	176	WFV4	13:07	12:55	12
19	180	WFV4	13:06	12:30	36
26	208	WFV4	12:59	12:55	4

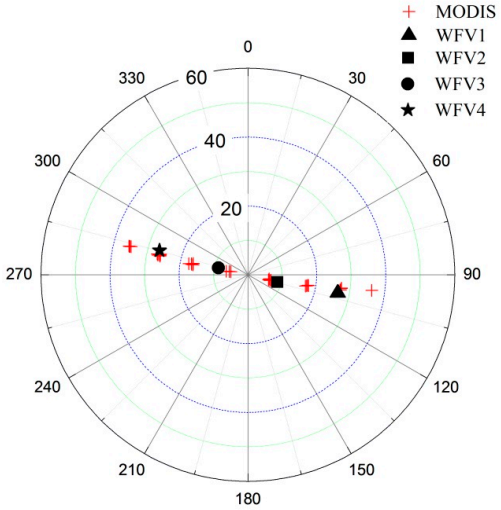

Figure 4. The view angles for the Dunhuang radiometric calibration sites (DRCS) in WFV and MODIS images.

3. Methodology

3.1. Brief Review of the RBA

The principle of the RBA is similar to that of the geometric block adjustment [20]. The regions associated with ground survey data, such as surface reflectance, aerosol optical thickness (AOT), BRDF, etc., act as the RCPs. Meanwhile, the spectrally-homogeneous regions in the overlap of adjacent cameras are treated as RTPs. The RBA model, therefore, is performed by combining both RCPs' and RTPs' information to not only achieve high absolute radiometric correction, but also minimize the radiometric difference between adjacent cameras [21].

Thus far, the feasibility and reliability of the RBA have been verified by many research words. Chandelier et al. described the process of RTPs' extraction and applied the RBA to correct the radiometric heterogeneities in aerial images due to atmospheric variations, temporal differences and surface BRDF [20]. In order to improve relative and absolute homogenization in aerial images, López et al. applied the RBA to Z/I-Imaging digital mapping camera (DMC) images. They used

not only RCPs to obtain calibration parameters from the camera and surface reflectance images, but also RTPs to correct the anisotropy caused by the BRDF of surfaces viewed under large observation angles with constant illumination [21]. Falala et al. implemented the RBA to improve the reference 3D production line in particular SPOT5 HRS images' mosaicking step, which dramatically reduced the radiometric difference between images [22]. Aimed at optimal adaptation of large blocks of Leica ADS line-scanner imagery for subsequent mosaicking, Gehrke used the RBA to provide homogenous radiometry throughout large areas [23]. Honkavaara et al. introduced the RBA to produce homogeneous data for non-homogeneous input UAV images for precision agriculture, which provided promising results for biomass estimation [24]. Yan et al. applied the RBA to three real airborne LiDAR data strips to reduce the systematic noises appearing in the overlapping region. The processing results showed that the overall accuracies were improved by up to 16.5% in the results of intensity data classification [25]. For generating seamless mosaics of aerial images obtained by different sensors, Gehrke and Beshah used the RBA to compensate radiometric differences based on RTPs, RCPs and image statistics [26]. Based on atmospheric radiative transfer (ART) models, pre-selected BRDF models and RCPs, the RBA was implemented for the digital radiometric model (DRM) and orthophoto mosaics showing no radiometric differences at the seam lines [27]. Although each flight line of the airborne LiDAR system had been calibrated independently by calibration coefficients, the radiances in the overlapping region had slightly different measurements. Therefore, the RBA was used to correct those radiometric differences [28].

Through the analysis of the previous research situation, it is shown that most of them apply the RBA method to the dodging process during the image splicing for aerial or SAR images. However, it should be judged whether the basic concept of the RBA method can be introduced into the on-orbit radiometric calibration or not.

3.2. On-Orbit Radiometric Calibration Model Based on the RBA

In this paper, the GF-1 WFV sensor, a typical multi-camera mosaic imaging sensor, is treated as the uncalibrated sensor, while MODIS acted as the reference. The on-orbit radiometric calibration model based on the RBA is designed, and the specific establishment steps are illustrated in Figure 5, including RCPs' information extraction, RTPs' information extraction, calibration model establishment, calibration coefficients' solution and accuracy validation. Figure 6 shows the sketch map of RCPs' and RTPs' distribution.

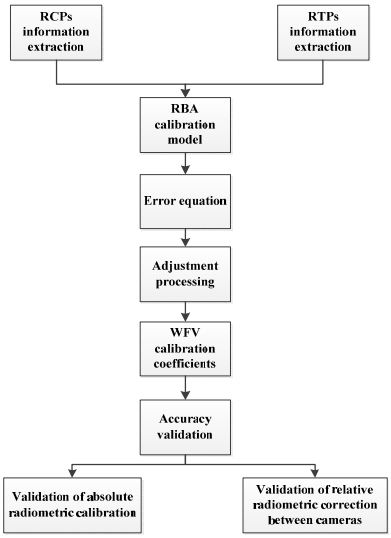

Figure 5. The flowchart of the on-orbit radiometric calibration model based on the radiometric block adjustment (RBA) method. RCP, radiometric control point; RTP, radiometric tie point.

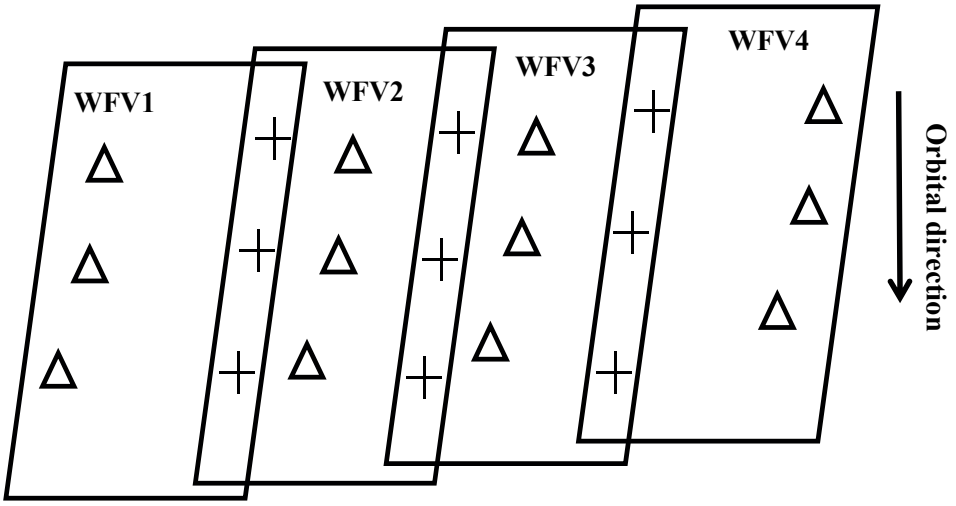

Figure 6. The sketch map of RCPs' (Δ) and RTPs' (+) distribution.

3.2.1. RCPs Information Extraction

It is a fundamental prerequisite for the RCPs' information extraction that the radiometric property of the investigated camera should be stable. Under this condition, we can use long-time series image pairs to transfer the radiometric property from the reference sensor to the candidate one. Therefore, we firstly analyze the four WFV cameras' radiation stability using those image pairs listed in Table 1. The center region of the DRCS is treated as the research area (94.2303°E, 40.2141°N). According to the geometric position information of MODIS and WFV, we choose a small window (5 × 5 pixels) on the MODIS image around the center region, fir which the corresponding window on the WFV image is up to 156 × 156 pixels due to the spatial resolution difference. DNs in both windows are averaged and normalized to the first one. The trends of normalized DN of both GF WFVs and MODIS at each band are depicted in Figure 7, showing a good consistency. To further quantitative analysis, the average relative different values between MODIS and each WFV camera are calculated. The relative difference is defined as "(Normalized DN of WFV − Normalized DN of MODIS)/Normalized DN of MODIS". Table 2 shows that the maximum average relative differences of WFV1, WFV2, WFV3 and WFV4 for each band are −1.82%, −2.02%, −1.70% and −1.21%, respectively, which proves that the radiometric property of the WFV camera is significantly stable during this operation period. Therefore, we can extract RCPs' information from those valid images.

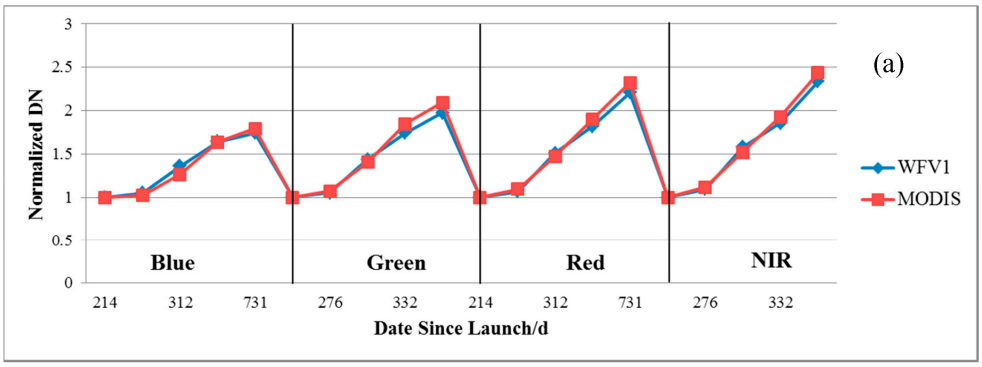

Figure 7. *Cont.*

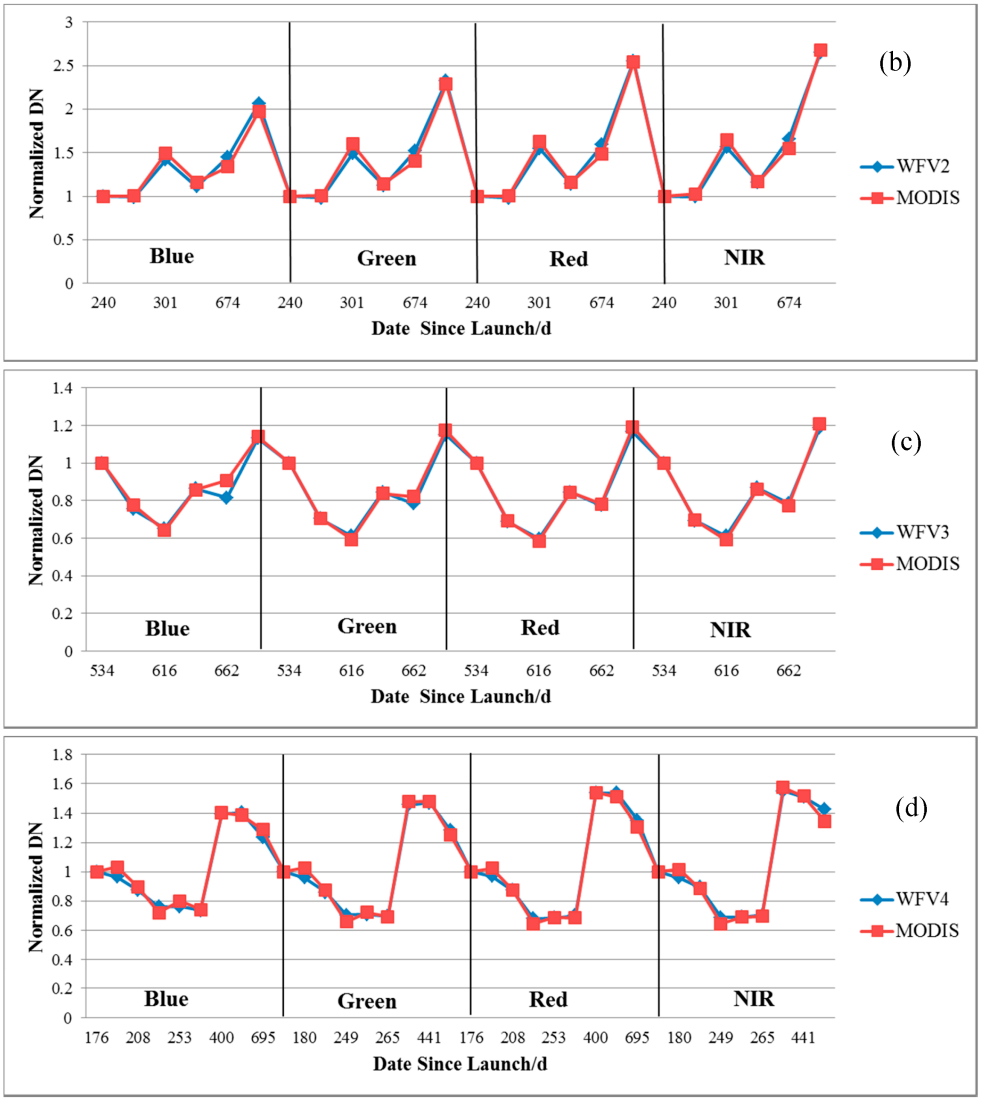

Figure 7. The trends of normalized DN of both GF WFVs and MODIS at each band. (**a**) WFV1 and MODIS; (**b**) WFV2 and MODIS; (**c**) WFV3 and MODIS; (**d**) WFV4 and MODIS.

Table 2. The relative difference of normalized DN for the WFV and MODIS images.

Camera	Blue	Green	Red	NIR
WFV1	1.45%	−2.02%	−1.70%	−1.21%
WFV2	0.36%	−0.29%	−0.08%	−0.37%
WFV3	−1.82%	−0.49%	−0.27%	0.72%
WFV4	−1.40%	−0.21%	0.83%	0.85%

RCPs information contains either average DN values (156 × 156 pixels) of the WFV sensor or average TOA radiances (5 × 5 pixels) of the MODIS sensor in the center region of the DRCS. The fundamental prerequisite for the radiometric calibration based on the RBA is the accurate extraction of RCPs' information. However, there are some factors that affect the accuracy of RCPs' information extraction within the cross-calibration method, such as geometric misregistrations, atmospheric characterization, different relative spectral responses (RSRs) the spectral signature of the ground target, BRDF, etc. [29–34].

Therefore, in view of these problems, a series of measures is employed to restrict and optimize the processing of RCPs' information extraction. Firstly, the DRCS possessing a good spectral homogeneous characteristic is chosen as the radiation delivery platform in order to reduce the influence of geometric registration errors [13]. Secondly, the synchronous AOT obtained either from MOD04 or MOD08 [8] are adopted in our approach. Thirdly, we use a spectral band adjustment factor (SBAF) to compensate the intrinsic offsets between two sensors caused by RSR mismatches [29]. At last, the historical radiometric profiles and the historical BRDF data of the DRCS are applied to substitute for simultaneous measurement data [15].

Through the above series of optimization measures, RCPs' information and the SBAF are extracted. Then, the equivalent TOA radiances of WFV are computed by Equation (1).

$$\mathrm{L}^{i}{}_{\mathrm{wfv}} = \mathrm{SBAF}^{i} \cdot \mathrm{L}^{i}{}_{\mathrm{MODIS}} \tag{1}$$

where $\mathrm{L}^{i}{}_{\mathrm{wfv}}$ and $\mathrm{L}^{i}{}_{\mathrm{MODIS}}$ are the equivalent TOA radiance of WFV and the TOA radiance of MODIS in the i-th band, respectively. SBAF^{i} is the SBAF of WFV and MODIS in the i-th band (i = 1, 2, 3 and 4).

3.2.2. RTPs' Information Extraction

Geometrical Misalignment Elimination

The overlaps of adjacent cameras have obvious geometrical misalignment due to the camera installation and satellite operation status, which affects the precision and efficiency of RTPs' information extraction. Therefore, geometric block adjustment of the four WFV images in the same orbit must be performed before the RTPs' information extraction,

However, the adjacent WFV cameras have weak convergence geometry whose convergent angle is less than 10°, which may cause an elevation error of hundreds of meters if using the traditional block adjustment. Therefore, DEM-aided block adjustment of RFM with weak convergence geometry, as in Equation (2), is applied to eliminate the geometrical misalignment, which can avoid the error equation appearing ill-conditioned [35]. The Aster G-DEM is used to provide the elevation information constraint.

$$\begin{bmatrix} V_s \\ V_l \end{bmatrix} = \begin{bmatrix} \frac{\partial F_s}{\partial e_0} & \frac{\partial F_s}{\partial e_1} & \frac{\partial F_s}{\partial e_2} & 0 & 0 & 0 & \frac{\partial F_s}{\partial \varphi} & \frac{\partial F_s}{\partial \lambda} \\ 0 & 0 & 0 & \frac{\partial F_l}{\partial f_0} & \frac{\partial F_l}{\partial f_1} & \frac{\partial F_l}{\partial f_2} & \frac{\partial F_l}{\partial \varphi} & \frac{\partial F_l}{\partial \lambda} \end{bmatrix} \begin{bmatrix} \Delta e_0 \\ \Delta e_1 \\ \Delta e_2 \\ \Delta f_0 \\ \Delta f_1 \\ \Delta f_2 \\ \Delta \varphi \\ \Delta \lambda \end{bmatrix} - \begin{bmatrix} S - \hat{S} \\ L - \hat{L} \end{bmatrix} \tag{2}$$

where V_s and V_l are the sample and row error, e_0, e_1, e_2, f_0, f_1 and f_2 are the affine transformation parameters in image plane, $\frac{\partial F}{\partial \varphi}$ and $\frac{\partial F}{\partial \lambda}$ are the first-order partial derivative of latitude and longitude, (S, L) is the image point coordinates after system error compensation and $(\hat{S}, \hat{L})$ is the initial image point coordinates projected by Rational Function Model (RFM).

RTPs' Extraction Standard

After geometrical misalignment elimination, the sliding window (11 pixels × 11 pixels) is introduced to find the spectrally-homogeneous surface where CV is less than the given threshold value in the overlapping region of a pair of adjacent cameras. Then, the averaged DN of this region is treated as the RTPs. During the RTPs' extraction processing, with respect to the radiation correlation of the adjacent camera in different response ranges, the RTPs are extracted from those images covering multiple land coverage types.

Radiometric Constraint Condition

The establishment of the radiometric constraint condition is the key issue of the proposed radiometric calibration method. For the overlapping region of adjacent cameras, most of the input parameters of 6S are the same or very close, such as sun and satellite observation angle, surface reflectance, BRDF, AOT, etc. However, the RSRs shown in Figure 2 have slight differences between WFV cameras, which may impact the final calibration accuracy. Then, 50 different spectral profiles from the USGS spectral library are taken as surface profiles to analyze the TOA radiance correlation of adjacent cameras in the whole RSR section by the simulative method. The main simulative parameters used in 6S for the overlapping region are listed in Table 3. The results are shown in Figure 8. It is clear that TOA radiance between two adjacent cameras has a very high linear correlation with R^2 close to one. Hence, the TOA radiance difference of adjacent cameras in overlap regions is ignored in our research.

Table 3. The main simulative parameters used in the 6S model for the overlapping region. AOT, aerosol optical thickness.

Parameters	Value
Sun zenith angle	30°
Sun azimuth angle	150°
Satellite zenith angle	17° for WFV1 and WFV2, 0° for WFV2 and WFV3, 17° for WFV3 and WFV4
Satellite azimuth angle	102° for WFV1 and WFV2, 193° for WFV2 and WFV3, 284° for WFV3 and WFV4
Atmospheric conditions	Mid-latitude Summer
Aerosol model	Continent
550-nm AOT	0.15
Altitude	1200 m
Surface profiles	50 different spectral profiles from the USGS spectral library

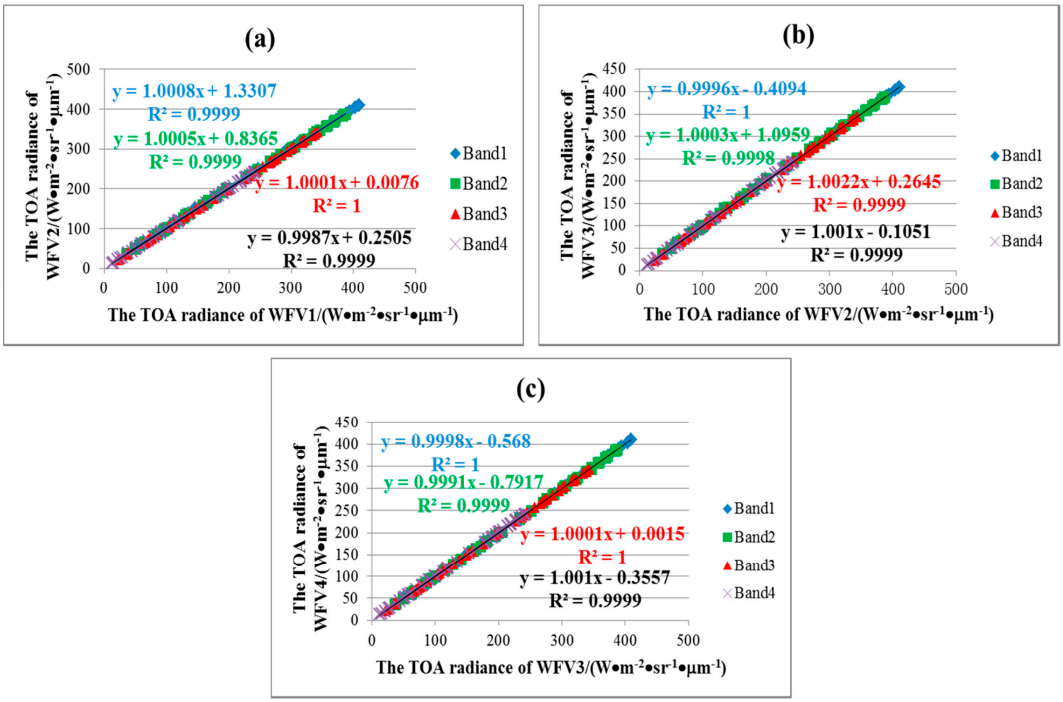

Figure 8. The TOA radiance correlation of the adjacent cameras. (**a**) WFV1 and WFV2; (**b**) WFV2 and WFV3; (**c**) WFV3 and WFV4.

3.2.3. Radiometric Calibration Model Establishment

This assumes that the number of the RCPs extracted from WFV1, WFV2, WFV3 and WFV4 is m, n, p and q. The number of the RTPs extracted from the overlapping regions of WFV1 and WFV2, WFV2

and WFV3, WFV3 and WFV4 is d, e and f. The radiometric calibration model based on the principle of the RBA in the *i*-th band can be found as Equation (3). Then, the unknown parameter matrix X is solved by the least square iterative method as Equation (4), when **dX** satisfies the convergence condition.

$$\mathbf{V} = \mathbf{AX} - \mathbf{L} \tag{3}$$

$$\mathbf{A} = \begin{bmatrix}
\mathrm{DN}_{(\mathrm{wfv1},i)}^{\mathrm{C}(1)} & 1 & 0 & 0 & 0 & 0 & 0 & 0 \\
\vdots & \vdots & \vdots & \vdots & \vdots & \vdots & \vdots & \vdots \\
\mathrm{DN}_{(\mathrm{wfv1},i)}^{\mathrm{C}(m)} & 1 & 0 & 0 & 0 & 0 & 0 & 0 \\
0 & 0 & \mathrm{DN}_{(\mathrm{wfv2},i)}^{\mathrm{C}(1)} & 1 & 0 & 0 & 0 & 0 \\
\vdots & \vdots & \vdots & \vdots & \vdots & \vdots & \vdots & \vdots \\
0 & 0 & \mathrm{DN}_{(\mathrm{wfv2},i)}^{\mathrm{C}(n)} & 1 & 0 & 0 & 0 & 0 \\
0 & 0 & 0 & 0 & \mathrm{DN}_{(\mathrm{wfv3},i)}^{\mathrm{C}(1)} & 1 & 0 & 0 \\
\vdots & \vdots & \vdots & \vdots & \vdots & \vdots & \vdots & \vdots \\
0 & 0 & 0 & 0 & \mathrm{DN}_{(\mathrm{wfv3},i)}^{\mathrm{C}(p)} & 1 & 0 & 0 \\
0 & 0 & 0 & 0 & 0 & 0 & \mathrm{DN}_{(\mathrm{wfv4},i)}^{\mathrm{C}(1)} & 1 \\
\vdots & \vdots & \vdots & \vdots & \vdots & \vdots & \vdots & \vdots \\
0 & 0 & 0 & 0 & 0 & 0 & \mathrm{DN}_{(\mathrm{wfv4},i)}^{\mathrm{C}(q)} & 1 \\
\mathrm{DN}_{(\mathrm{wfv1},i)}^{\mathrm{T}(\mathrm{wfv1,wfv2},1)} & 1 & -\mathrm{DN}_{(\mathrm{wfv2},i)}^{\mathrm{T}(\mathrm{wfv1,wfv2},1)} & -1 & 0 & 0 & 0 & 0 \\
\vdots & \vdots & \vdots & \vdots & \vdots & \vdots & \vdots & \vdots \\
\mathrm{DN}_{(\mathrm{wfv1},i)}^{\mathrm{T}(\mathrm{wfv1,wfv2},d)} & 1 & -\mathrm{DN}_{(\mathrm{wfv2},i)}^{\mathrm{T}(\mathrm{wfv1,wfv2},d)} & -1 & 0 & 0 & 0 & 0 \\
0 & 0 & \mathrm{DN}_{(\mathrm{wfv2},i)}^{\mathrm{T}(\mathrm{wfv2,wfv3},1)} & 1 & -\mathrm{DN}_{(\mathrm{wfv3},i)}^{\mathrm{T}(\mathrm{wfv2,wfv3},1)} & -1 & 0 & 0 \\
\vdots & \vdots & \vdots & \vdots & \vdots & \vdots & \vdots & \vdots \\
0 & 0 & \mathrm{DN}_{(\mathrm{wfv2},i)}^{\mathrm{T}(\mathrm{wfv2,wfv3},e)} & 1 & -\mathrm{DN}_{(\mathrm{wfv3},i)}^{\mathrm{T}(\mathrm{wfv2,wfv3},e)} & -1 & 0 & 0 \\
0 & 0 & 0 & 0 & \mathrm{DN}_{(\mathrm{wfv3},i)}^{\mathrm{T}(\mathrm{wfv3,wfv4},1)} & 1 & -\mathrm{DN}_{(\mathrm{wfv4},i)}^{\mathrm{T}(\mathrm{wfv3,wfv4},1)} & -1 \\
\vdots & \vdots & \vdots & \vdots & \vdots & \vdots & \vdots & \vdots \\
0 & 0 & 0 & 0 & \mathrm{DN}_{(\mathrm{wfv3},i)}^{\mathrm{T}(\mathrm{wfv3,wfv4},f)} & 1 & -\mathrm{DN}_{(\mathrm{wfv4},i)}^{\mathrm{T}(\mathrm{wfv3,wfv4},f)} & -1
\end{bmatrix} \tag{4}$$

$$\mathbf{L} = \begin{bmatrix} \mathrm{L}_{(\mathrm{wfv1},i)}^{\mathrm{C}(1)} & \cdots & \mathrm{L}_{(\mathrm{wfv1},i)}^{\mathrm{C}(m)} & \mathrm{L}_{(\mathrm{wfv2},i)}^{\mathrm{C}(1)} & \cdots & \mathrm{L}_{(\mathrm{wfv2},i)}^{\mathrm{C}(n)} & \mathrm{L}_{(\mathrm{wfv3},i)}^{\mathrm{C}(1)} & \cdots & \mathrm{L}_{(\mathrm{wfv3},i)}^{\mathrm{C}(p)} & \mathrm{L}_{(\mathrm{wfv4},i)}^{\mathrm{C}(1)} & \cdots & \mathrm{L}_{(\mathrm{wfv4},i)}^{\mathrm{C}(q)} & 0 \ \cdots \ 0 & 0 \ \cdots \ 0 & 0 \ \cdots \ 0 \end{bmatrix}^T$$

$$\mathbf{X} = \begin{bmatrix} \mathrm{G}_{\mathrm{wfv1}}^{i} & \mathrm{O}_{\mathrm{wfv1}}^{i} & \mathrm{G}_{\mathrm{wfv2}}^{i} & \mathrm{O}_{\mathrm{wfv2}}^{i} & \mathrm{G}_{\mathrm{wfv3}}^{i} & \mathrm{O}_{\mathrm{wfv3}}^{i} & \mathrm{G}_{\mathrm{wfv4}}^{i} & \mathrm{O}_{\mathrm{wfv4}}^{i} \end{bmatrix}^T$$

$$\mathbf{dX} = (\mathbf{A}^{\mathrm{T}}\mathbf{A})^{-1}\mathbf{A}^{\mathrm{T}}\mathbf{L}$$

where **A**, **L**, **X** and **V** are the coefficient matrix, constant matrix, unknown parameter matrix and residual matrix, respectively. $\mathrm{DN}_{(\mathrm{wfv1},i)}^{\mathrm{C}(m)}$ and $\mathrm{L}_{(\mathrm{wfv1},i)}^{\mathrm{C}(m)}$ are the DN and TOA radiance of the *m*-th RCPs of WFV1 image in the *i*-th band. $\mathrm{DN}_{(\mathrm{wfv1},i)}^{\mathrm{T}(\mathrm{wfv1,wfv2},d)}$ is the DN of the *d*-th RTPs of WFV1 image in the *i*-th band in the overlapping region of the WFV1 and WFV2 cameras. $\mathrm{G}_{\mathrm{wfv1}}^{i}$ and $\mathrm{O}_{\mathrm{wfv1}}^{i}$ are the gain and offset of absolute radiometric calibration coefficients of WFV1 in the *i*-th band. The other parameters have similar meanings.

4. Results

4.1. Calibration Results

According to the RCPs, RTPs and the proposed radiometric calibration method, the on-orbit radiometric calibration coefficients of the four WFV cameras of the GF-1 satellite are calculated and listed in Table 4.

Table 4. On-orbit radiometric calibration coefficients of the WFV sensor calibrated by RBA ($\mathrm{W{\cdot}m^{-2}{\cdot}sr^{-1}{\cdot}\mu m^{-1}}$).

Band	WFV1		WFV2		WFV3		WFV4	
	Gain	Offset	Gain	Offset	Gain	Offset	Gain	Offset
1	0.1723	3.9090	0.1699	6.4417	0.1725	6.1388	0.1740	3.4047
2	0.1442	0.4192	0.1414	1.6595	0.1581	2.5134	0.1598	-0.2751
3	0.1239	-0.3238	0.1211	0.2630	0.1345	0.9027	0.1353	1.6649
4	0.1359	2.2127	0.1334	2.4679	0.1373	2.8715	0.1340	2.7709

4.2. Validation of Absolute Radiometric Calibration

In order to validate the absolute radiometric calibration accuracy of the proposed method coefficients (PMCs), the valid MODIS and WFV images covering other different surfaces at different times are collected. Then, the check points (CKPs), about 166 for WFV1, 109 for WFV2, 144 for WFV3 and 278 for WFV4, are selected from those image pairs including grass, water, concrete, salt lick, soil, farmland, etc. The DNs of WFV and the corresponding TOA radiance of MODIS are obtained on the base of the geographic coordinates. The TOA radiances derived by the PMCs are compared with TOA radiance of MODIS. The relative errors (REs) are calculated by Equation (5). Finally, the results are summarized in Table 5, which illustrates that the PMCs have high radiometric calibration accuracy. The average REs of each band are 6.35%, 5.05%, 5.28% and 6.05%.

$$\mathrm{RE}^i = ABS(\mathrm{L}^i_{\mathrm{wfv}} - \mathrm{L}^i_{\mathrm{MODIS}})/\mathrm{L}^i_{\mathrm{MODIS}} \times 100\% \quad (5)$$

where RE^i is the relative error in the *i*-th band, $\mathrm{L}^i{}_{\mathrm{wfv}}$ is the TOA radiance of the WFV image calculated by the PMCs in the *i*-th band, $\mathrm{L}^i{}_{\mathrm{MODIS}}$ is the TOA radiances of MODIS in the *i*-th band and *ABS*( ) is the absolute value function.

Table 5. The RE of on-orbit radiometric calibration coefficients calibrated by RBA.

Camera	RE/%			
	Band 1	**Band 2**	**Band 3**	**Band 4**
WFV1	6.61	7.02	4.45	6.82
WFV2	7.91	4.91	5.16	7.61
WFV3	4.39	3.43	4.84	4.02
WFV4	6.50	4.84	6.67	5.76

4.3. Validation of Relative Radiometric Correction between Cameras

In order to estimate the effect and accuracy of the relative radiometric correction between cameras based on the PMCs, the CKPs are extracted from the overlapping regions of adjacent camera images in the same orbit at different phases. Then, the TOA radiances are calculated by both the PMCs and the OCCs. Figures 9–11 illustrate the average absolute values of the TOA radiance differences of CKPs. In Table 6, the radiometric differences calculated with the PMCs are reduced to 1.12, 1.06, 1.04 and 1.34 $\mathrm{W{\cdot}m^{-2}{\cdot}sr^{-1}{\cdot}\mu m^{-1}}$ for four bands in the overlapping region between WFV1 and WFV2; and to 0.80, 0.93, 0.64 and 0.71 $\mathrm{W{\cdot}m^{-2}{\cdot}sr^{-1}{\cdot}\mu m^{-1}}$ for four bands in the overlapping region between WFV3 and WFV4, which is significantly less than the differences calculated with both the 2013 OCCs and 2014 OCCs. Only radiometric differences between WFV2 and WFV3 calculated from 2014 OCCs are comparative to the values from the PMCs. Statistical results reveal that better relative radiometric correction between cameras can be achieved with PMCs than the OCCs currently issued.

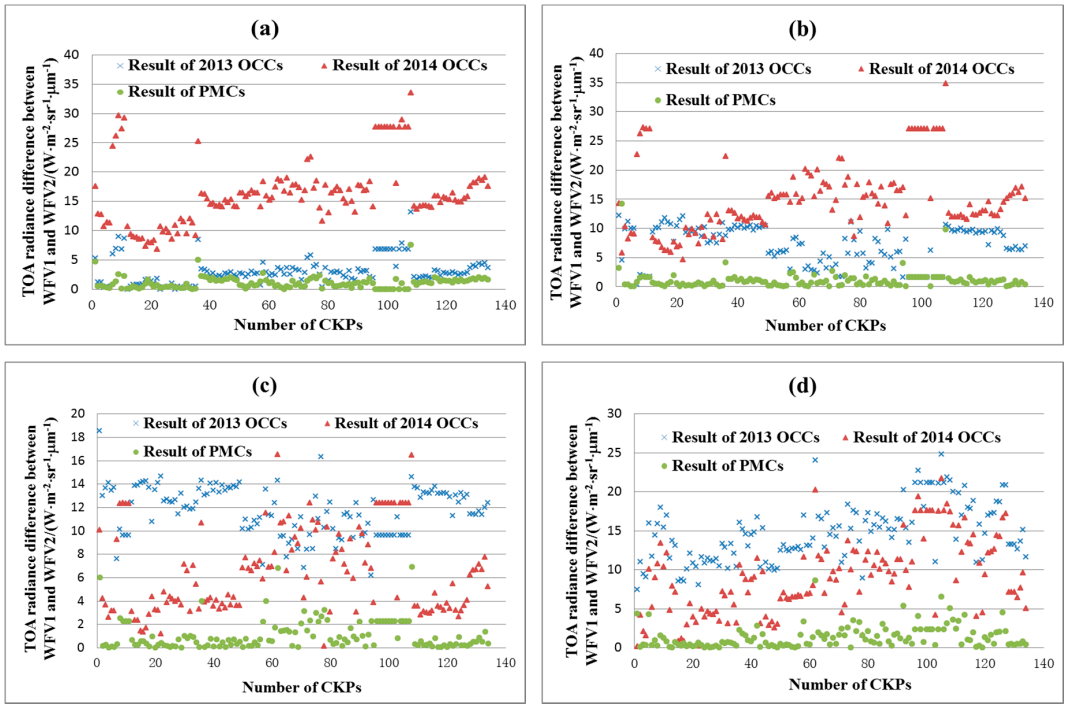

Figure 9. TOA radiance differences of check points (CKPs) in WFV1 and WFV2. PMC, proposed method coefficient; OCC, official calibration coefficient. (**a**) Band1; (**b**) Band2; (**c**) Band3; (**d**) Band4.

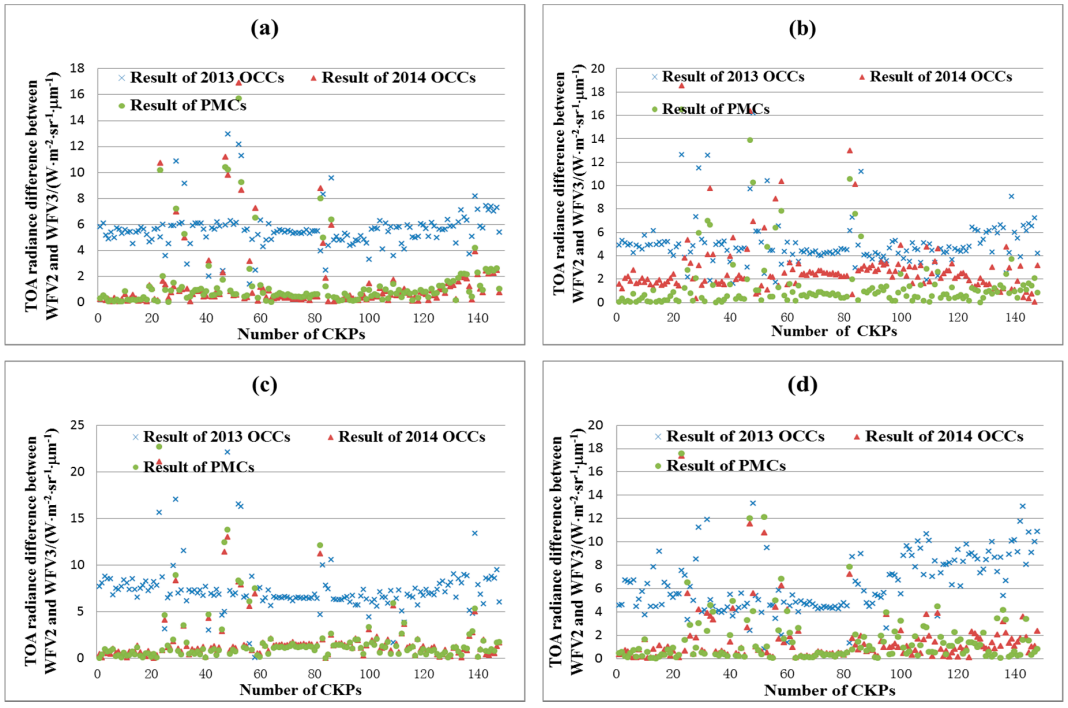

Figure 10. TOA radiance differences of CKPs in WFV2 and WFV3. (**a**) Band1; (**b**) Band2; (**c**) Band3; (**d**) Band4.

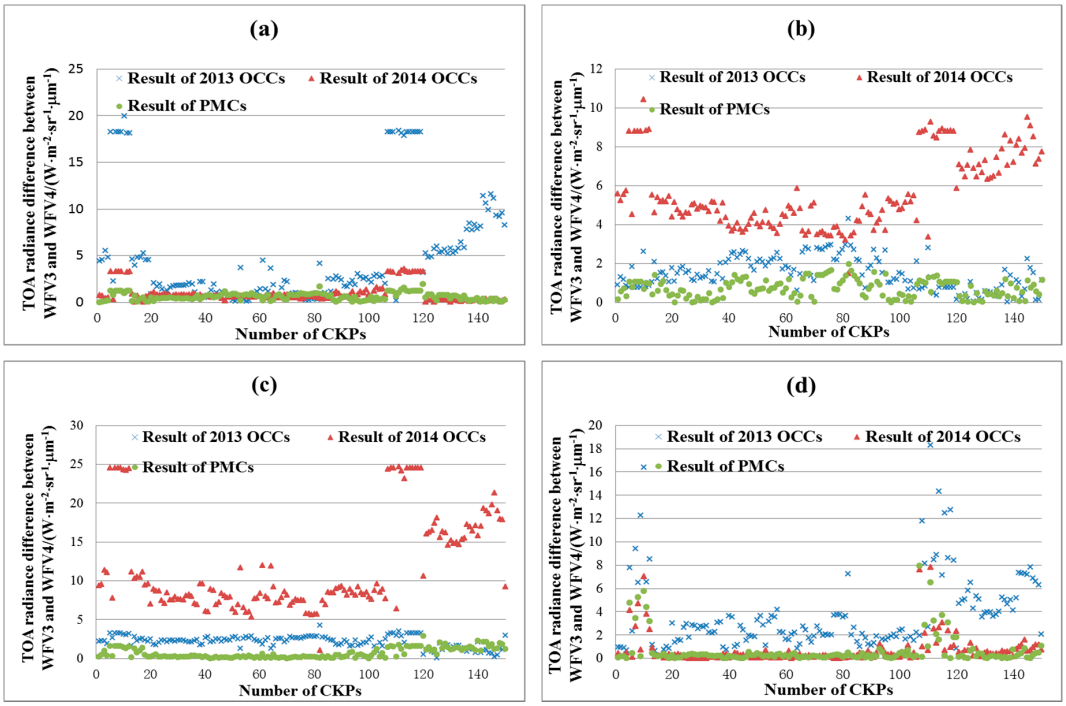

Figure 11. TOA radiance differences of CKPs in WFV3 and WFV4. (**a**) Band1; (**b**) Band2; (**c**) Band3; (**d**) Band4.

Table 6. Average absolute value of TOA radiance differences of CKPs.

Overlaps	Results	Average Absolute Value of Difference ($W \cdot m^{-2} \cdot sr^{-1} \cdot \mu m^{-1}$)			
		Band 1	Band 2	Band 3	Band 4
WFV1 and WFV2	2013 OCCs results	3.08	7.10	11.79	14.75
	2014 OCCs results	16.45	15.02	6.53	9.09
	PMCs results	1.12	1.06	1.04	1.34
WFV2 and WFV3	2013 OCCs results	5.56	5.00	7.32	6.35
	2014 OCCs results	1.30	2.82	1.80	1.44
	PMCs results	1.39	1.43	1.76	1.50
WFV3 and WFV4	2013 OCCs results	6.05	1.47	2.36	4.46
	2014 OCCs results	1.17	6.08	10.61	0.93
	PMCs results	0.80	0.93	0.64	0.71

5. Discussion

5.1. Each WFV Camera Calibrated by the Cross-Calibration Method Independently

In order to compare the results calculated by the RBA to obtain the calibration coefficients for four WFVs simultaneously and by the traditional cross-calibration method to calculate WFV calibration coefficients separately, this research uses the same RCPs extracted from the images listed in Table 1 to get the radiometric calibration coefficients of each WFV sensor independently.

Figure 12 shows that R^2 is very close to one, which proves the linear fitting accuracy is very high. On-orbit radiometric calibration coefficients of four WFVs calibrated by the cross-calibration method and the REs are listed in Table 7. The average RE of each band is 6.20%, 4.36%, 5.11% and 5.29%, which are slightly superior to that of the RBA. However, Table 8 shows that the average absolute values of TOA radiance differences of CKPs are larger than those from the RBA. The average TOA radiance differences of each band rises about 36.79%, 64.27%, 55.29% and 44.61%. Although the absolute radiometric calibration accuracy of the RBA is slightly lower than that of the regular

cross-calibration method, the RBA can provide the relative radiometric correction between cameras with higher accuracy and hence provide better measurements supporting quantitative remote sensing for a large application area.

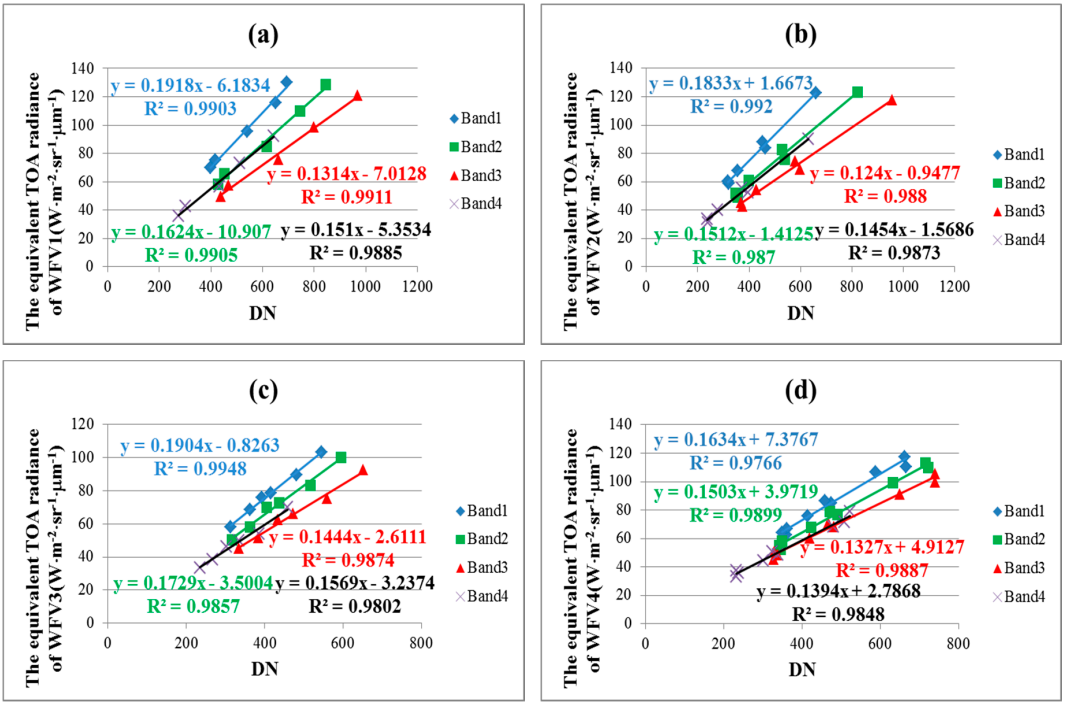

Figure 12. Each WFV camera calibrated by the cross-calibration method. (**a**) WFV1; (**b**) WFV2; (**c**) WFV3; (**d**) WFV4.

Table 7. On-orbit radiometric calibration coefficients of WFV sensor calibrated by cross-calibration method and the RE.

Camera		Band 1	Band 2	Band 3	Band 4
WFV1	Gain/W·m^{-2}·sr^{-1}·μm^{-1}	0.1918	0.1624	0.1314	0.1510
	Offset/W·m^{-2}·sr^{-1}·μm^{-1}	−6.1834	−10.907	−7.0128	−5.3534
	RE/%	6.59	5.66	6.14	5.32
WFV2	Gain/W·m^{-2}·sr^{-1}·μm^{-1}	0.1833	0.1512	0.1240	0.1454
	Offset/W·m^{-2}·sr^{-1}·μm^{-1}	1.6673	−1.4125	−0.9477	−1.5686
	RE/%	6.13	4.26	4.89	7.98
WFV3	Gain/W·m^{-2}·sr^{-1}·μm^{-1}	0.1904	0.1729	0.1444	0.1569
	Offset/W·m^{-2}·sr^{-1}·μm^{-1}	−0.8263	−3.5004	−2.6111	−3.2374
	RE/%	5.84	3.29	3.96	3.25
WFV4	Gain/W·m^{-2}·sr^{-1}·μm^{-1}	0.1634	0.1503	0.1327	0.1394
	Offset/W·m^{-2}·sr^{-1}·μm^{-1}	7.3767	3.9719	4.9127	2.7868
	RE/%	6.22	4.24	5.43	4.61

Table 8. Average absolute value of TOA radiance differences of CKPs.

Overlaps	Average Absolute Value of Difference (W·m^{-2}·sr^{-1}·μm^{-1})			
	Band 1	Band 2	Band 3	Band 4
WFV1 and WFV2	1.68	3.82	2.95	2.12
WFV2 and WFV3	1.35	2.63	2.27	1.94
WFV3 and WFV4	4.00	3.71	3.00	2.77

5.2. Uncertainty Caused by RCPs Distribution

The above calibration coefficients in Table 3 calculated based on the RBA use all the RCPs' information extracted from four cameras' images. However, more investigations are required to determine whether the RCPs' distribution may affect the calibration accuracy. Consequently, we set the different distribution schemes to discuss the influence of this factor on absolute radiometric calibration and relative radiometric correction.

As shown in Table 9, the conclusions can be summarized as follows:

1. On the whole, the REs of the calibration coefficients for each WFV camera are down or stable at a small value when using more RCPs located in different WFV cameras. Taking the WFV1 camera as an example, the REs of each band become lower from 8.39%, 8.78%, 4.89% and 14.95% to 6.61%, 7.91%, 4.39% and 6.50%. This is because more RCPs extracted from different cameras can effectively reduce the calibration uncertainty.
2. The REs of the WFV1 camera calculated by the RBA only with RCPs in the WFV1 camera are larger than that of the WFV1 camera calculated by cross-calibration listed in Table 6. The reason may be that the different accuracies and distributions of RTPs in different overlapping regions have an impact on the absolute radiometric calibration to some degree. However, when not all WFV cameras have RCPs, although the calibration coefficients calculated by RBA have slightly larger REs than those of the traditional cross-calibration, except for the near-infrared band, the RBA can obtain the calibration coefficients of other cameras without RCPs based on the radiometric constraint condition between the adjacent cameras.
3. Only four cameras' RCPs are introduced in the RBA model, the REs of all cameras become lower in the near-infrared band. However, the REs of the first three bands are all less than 8.78% even if only one camera's RCPs are used. This is probably because the hypothesis is more suitable for the first three bands so that the actual radiometric performance differences of different cameras in the same band can be neglected.

Table 9. The REs of the calibration coefficients caused by the RCPs' distribution.

RCPs Position	Band	RE/%			
		WFV1	WFV2	WFV3	WFV4
WFV1	1	8.39	8.06	4.35	4.48
	2	8.78	6.25	6.18	3.89
	3	4.89	5.45	6.21	7.32
	4	14.95	15.52	36.03	7.52
WFV1 and WFV2	1	6.95	7.09	4.00	5.63
	2	8.07	5.51	5.20	3.96
	3	4.6	5.16	5.62	6.94
	4	10.89	10.5	28.35	6.22
WFV1, WFV2 and WFV3	1	6.35	6.78	4.22	6.30
	2	7.02	4.64	4.05	4.49
	3	4.48	5.11	5.52	6.67
	4	10.40	9.66	23.84	6.22
WFV1, WFV2, WFV3 and WFV4	1	6.61	7.02	4.45	6.28
	2	7.91	4.91	5.16	7.61
	3	4.39	3.43	4.84	4.02
	4	6.50	4.84	6.67	5.76

Table 10 shows the relative radiometric correction accuracy when using different RCPs from different cameras. It indicates that whatever the distribution, the average absolute values of the radiometric differences in four bands are all less than 1.77 $W \cdot m^{-2} \cdot sr^{-1} \cdot \mu m^{-1}$, which is smaller than most values in Table 8 obtained by the cross-calibration method. Therefore, the RBA method can effectively reduce the radiometric differences in the overlapping region of the adjacent camera.

Meanwhile, it manifests that the radiometric differences are slightly larger when more RCPs are introduced. It might be that when only one camera's RCPs are used to get all cameras' calibration coefficients, the other three cameras' calibration coefficients only depend on the radiometric correlation of the RTPs. However, as the number of RCPs increases, the computational procedure of those calibration coefficients will take into account the absolute radiometric constraint of RCPs in different cameras to some extent.

Table 10. The relative radiometric correction accuracy caused by the RCPs' distribution.

RCPs Position	Band	Average Absolute Value of Difference ($W \cdot m^{-2} \cdot sr^{-1} \cdot \mu m^{-1}$)		
		WFV1 and WFV2	WFV2 and WFV3	WFV3 and WFV4
WFV1	1	1.06	1.39	0.77
	2	0.94	1.38	0.91
	3	0.76	1.75	0.63
	4	0.95	1.33	0.61
WFV1 and WFV2	1	1.08	1.46	0.81
	2	0.97	1.43	0.95
	3	0.77	1.77	0.64
	4	1.01	1.49	0.69
WFV1, WFV2 and WFV3	1	1.14	1.47	0.82
	2	0.99	1.45	0.96
	3	0.80	1.77	0.64
	4	1.21	1.50	0.70
WFV1, WFV2, WFV3 and WFV4	1	1.12	1.39	0.80
	2	1.06	1.43	0.93
	3	1.04	1.76	0.64
	4	1.34	1.50	0.71

6. Summary and Conclusions

Taking the GF-1 WFV sensor as an object of investigation, an innovative on-orbit radiometric calibration method is proposed for the space-borne multi-camera mosaic imaging sensor to realize the integrated processing of on-orbit absolute radiometric calibration and relative radiometric correction between cameras. In our method, the RCPs are extracted from long-term valid WFV and MODIS image pairs at DRCS. After eliminating the geometrical misalignment with the DEM-aided block adjustment of the RFM method, the RTPs are automatically extracted from overlaps of WFV images at the same orbit. Then, the RCPs and RTPs are plugged into the calibration model, and the radiometric calibration coefficients are calculated by the least square method.

Compared with the results calculated with 2013 and 2014 OCCs, the radiometric calibration coefficients from our method not only achieve high absolute radiometric calibration accuracy for four WFVs, but also fulfill the relative radiometric correction between adjacent WFV cameras. Although the absolute radiometric calibration accuracy of WFVs from the proposed method is slightly lower than that calculated with the cross-calibration method for four WFVs separately, the radiometric differences in the overlapping regions between adjacent cameras are significantly improved, which is invaluable for an application area larger than the swath of a single camera. Meanwhile, after analyzing the influence of RCPs' distribution on the calibration results, we find that the location of RCPs obviously affects the absolute radiometric calibration accuracy especially for the near-infrared band, but has little impact on relative radiometric correction between cameras.

In the future, we will analyze the influence of RTPs on the calibration results to further optimize the calibration scheme and improve on-orbit radiometric calibration accuracy of the multi-camera mosaic imaging sensor.

Acknowledgments: The GF-1 WFV imagery at the Dunhuang test site used in this research is supported by the China Centre for Resources Satellite Data and Application (http://www.cresda.com/CN/). The MODIS data were downloaded from the Level 1 and Atmosphere Archive and Distribution System (https://earthdata.nasa.gov/about/daacs/daac-laads). The spectral profiles were downloaded from USGS Spectral Library (https://speclab.cr.usgs.gov/spectral-lib.html). This work was supported in part by the National Natural Science Foundation of China (No. 41671345); the General Manual for High Resolution Earth Observation System (No. 50-Y20A07-0508-15/16); Science and Technology of Henan Province (No. 172102210463); the National Key Research Program of China (No. 2016YFB0502500); the Scientific Research Foundation for the Talent, Nanjing University of Information Science & Technology.

Author Contributions: Yong Xie designed the research, carried out the modeling and prepared the manuscript. All authors contributed to the scientific content, the interpretation of the results and manuscript revisions.

Conflicts of Interest: The authors declare no conflict of interest.

References

1. Thome, K.J. Absolute radiometric calibration of Landsat 7 ETM+ using the reflectance-based method. *Remote Sens. Environ.* **2001**, *78*, 27–38. [CrossRef]
2. Chander, G.; Markham, B. Revised Landsat-5 TM radiometric calibration procedures and postcalibration dynamic ranges. *IEEE Trans. Geosci. Remote Sens.* **2003**, *41*, 2674–2677. [CrossRef]
3. Mishra, N.; Helder, D.; Angal, A.; Choi, J.; Xiong, X. Absolute calibration of optical satellite sensors using Libya 4 pseudo invariant calibration site. *Remote Sens.* **2014**, *6*, 1327–1346. [CrossRef]
4. Thome, K.J.; Hekder, D.L.; Aaron, D.; Dewald, J.D. Landsat-5 TM and Landsat-7 ETM+ absolute radiometric calibration using the reflectance-based method. *IEEE Trans. Geosci. Remote Sens.* **2004**, *42*, 2777–2785. [CrossRef]
5. Gao, H.; Gu, X.; Yu, T.; Sun, Y.; Liu, Q. Cross-calibration of gf-1 pms sensor with landsat 8 oli and terra modis. *IEEE Trans. Geosci. Remote Sens.* **2016**, *54*, 4847–4854. [CrossRef]
6. Xiong, X.; Barnes, W. An overview of MODIS radiometric calibration and characterization. *Adv. Atmos. Sci.* **2006**, *23*, 69–79. [CrossRef]
7. Xiong, X.; Sun, J.; Barnes, W.; Salomonson, V.; Esposito, J.; Erives, H.; Guenther, B. Multiyear on-orbit calibration and performance of terra MODIS reflective solar bands. *IEEE Trans. Geosci. Remote Sens.* **2007**, *45*, 879–889. [CrossRef]
8. Han, J.; Xie, Y. Image dodging algorithm for gf-1 satellite wfv imagery. *Acta Geodaeticaet Cartogr. Sin.* **2016**, *45*, 1423–1433.
9. Du, Y.; Cihlar, J.; Beaubien, J.; Latifovic, R. Radiometric normalization, compositing, and quality control for satellite high resolution image mosaics over large areas. *IEEE Trans. Geosci. Remote Sens.* **2001**, *39*, 623–634.
10. Zhang, Y.; Yu, L.; Sun, M.; Zhu, X. A mixed radiometric normalization method for mosaicking of high-resolution satellite imagery. *IEEE Trans. Geosci. Remote Sens.* **2017**, *55*, 2972–2984. [CrossRef]
11. Gao, H.; Gu, X.; Yu, T.; Li, L.; Sun, Y.; Xie, Y.; Liu, Q. Validation of the calibration coefficient of the gaofen-1 pms sensor using the landsat 8 Oli. *Remote Sens.* **2016**, *8*, 132. [CrossRef]
12. Bai, Z. The Technical Characteristics of GF-1 Satellite. *Aerospace China* **2013**, 5–9. (In Chinese)
13. Hu, X.; Liu, J.; Sun, L.; Rong, Z.; Li, Y.; Zhang, Y.; Zheng, Z.; Wu, R.; Zhang, L.; Gu, X. Characterization of CRCS dunhuang test site and vicarious calibration utilization for fengyun (FY) series sensors. *Can. J. Remote Sens.* **2010**, *36*, 566–582. [CrossRef]
14. Liu, J.; Li, Z. A new method for cross-calibration of two satellite sensors. *Int. J. Remote Sens.* **2004**, *25*, 5267–5281. [CrossRef]
15. Wang, Z.; Xiao, P.; Gu, X.; Feng, X.; Li, X.; Gao, H.; Li, H.; Lin, J.; Zhang, X. Uncertainty analysis of cross-calibration for hj-1 CCD camera. *Sci. China Tech. Sci.* **2013**, *56*, 713–723. [CrossRef]
16. Sun, L.; Hu, X.; Guo, M.; Xu, N. Multisite calibration tracking for FY-3A MERSI solar bands. *IEEE Trans. Geosci. Remote Sens.* **2012**, *50*, 4929–4942. [CrossRef]
17. Chen, Y.; Sun, K.; Li, D.; Bai, T.; Huang, C. Radiometric cross-calibration of gf-4 pms sensor based on assimilation of landsat-8 oli images. *Remote Sens.* **2017**, *9*, 811. [CrossRef]
18. Chen, S.; Zhang, T. An improved cloud masking algorithm for MODIS ocean colour data processing. *Remote Sens. Lett.* **2015**, *6*, 218–227. [CrossRef]

19. Wolfe, R.E.; Nishihama, M.; Fleig, A.J.; Kuyper, J.A.; Roy, D.P.; Storey, J.C.; Patt, F.S. Achieving sub-pixel geolocation accuracy in support of MODIS land science. *Remote Sens. Environ.* **2002**, *83*, 31–49. [CrossRef]
20. Chandelier, L.; Martinoty, G. Radiometric aerial triangulation for the equalization of digital aerial images and orthoimages. *Photogramm. Eng. Remote Sens.* **2009**, *75*, 193–200. [CrossRef]
21. López, D.H.; García, B.F.; Piqueras, J.G.; Alcázar, G.V. An approach to the radiometric aerotriangulation of photogrammetric images. *ISPRS J. Photogramm. Remote Sens.* **2011**, *66*, 883–893. [CrossRef]
22. Falala, L.; Gachet, R.; Cunin, L. Radiometric block-adjustment of satellite images reference3D production line improvement. In Proceedings of the XXI ISPRS Congress, Beijing, China, 3–11 July 2008.
23. Gehrke, S. Radiometric processing of ADS imagery: Mosaicking of large image blocks. In Proceedings of the ASPRS Annual Conference, San Diego, CA, USA, 26–30 April 2010.
24. Honkavaara, E.; Saari, H.; Kaivosoja, J.; Pölönen, I.; Hakala, T.; Litkey, P.; Mäkynen, J.; Pesonen, L. Processing and assessment of spectrometric, stereoscopic imagery collected using a lightweight uav spectral camera for precision agriculture. *Remote Sens.* **2013**, *5*, 5006–5039. [CrossRef]
25. Yan, W.; Shaker, A. Radiometric correction and normalization of airborne LIDAR intensity data for improving land-cover classification. *IEEE Trans. Geosci. Remote Sens.* **2014**, *52*, 7658–7673.
26. Gehrke, S.; Beshah, B. Radiometric normalization of large airborne image data sets acquired by different sensor types. In Proceedings of the XXIII ISPRS Congress, Prague, Czech Republic, 12–19 July 2016.
27. Pros, A.; Colomina, I.; Navarro, J.A.; Antequera, R.; Andrinal, P. Radiometric block adjustment and digital radiometric model generation. In Proceedings of the ISPRS Hannover Workshop 2013, Hannover, Germany, 21–24 May 2013.
28. Teo, T.A.; Wu, H.M. Radiometric block adjustment for multi-strip airborne waveform lidar data. *Remote Sens.* **2015**, *7*, 16831–16848. [CrossRef]
29. Chander, G.; Mishra, N.; Helder, D.L.; Aaron, D.B.; Angal, A.; Choi, T.; Xiong, X.; Doelling, D.R. Applications of spectral band adjustment factors (SBAF) for cross-calibration. *IEEE Trans. Geosci. Remote Sens.* **2013**, *51*, 1267–1281. [CrossRef]
30. Lachérade, S.; Fougnie, B.; Henry, P.; Gamet, P. Cross calibration over desert sites: Description, methodology, and operational implementation. *IEEE Trans. Geosci. Remote Sens.* **2013**, *51*, 1098–1113. [CrossRef]
31. Yang, A.; Zhong, B.; Lv, W.; Wu, S.; Liu, Q. Cross-calibration of GF-1/WFV over a desert site using Landsat-8/OLI imagery and ZY-3/TLC data. *Remote Sens.* **2015**, *7*, 10763–10787. [CrossRef]
32. Teillet, P.M.; Fedosejevs, G.; Thome, K.J.; Barker, J.L. Impacts of spectral band difference effects on radiometric cross-calibration between satellite sensors in the solar-reflective spectral domain. *Remote Sens. Environ.* **2007**, *110*, 393–409. [CrossRef]
33. Chander, G.; Helder, D.L.; Aaron, D.; Mishra, N.; Shrestha, A.K. Assessment of spectral, misregistration, and spatial uncertainties inherent in the cross-calibration study. *IEEE Trans. Geosci. Remote Sens.* **2013**, *51*, 1282–2196. [CrossRef]
34. Gao, H.; Gu, X.; Yu, T.; Li, X.; Gong, H.; Li, J. Time-series calibration for ccd camera: Taking cbers02b satellite as an example. *Acta Geodaeticaet Cartogr. Sin.* **2011**, *40*, 180–187.
35. Tong, X.; Liu, S.; Weng, Q. Bias-corrected rational polynomial coefficients for high accuracy geo-positioning of QuickBird stereo imagery. *ISPRS J. Photogramm. Remote Sens.* **2010**, *65*, 218–226. [CrossRef]